https://doi.org/10.5194/amt-2021-428
Preprint. Discussion started: 14 February 2022

Atmospheric Measurement Techniques Discussions

Quantifying the coastal urban surface layer structure using distributed temperature sensing in Helsinki, Finland

Sasu Karttunen[1], Ewan O'Connor[2], Olli Peltola[2,3], and Leena Järvi[1,4]

[1]Institute for Atmospheric and Earth System Research / Physics, Faculty of Science, 00014, University of Helsinki, Finland
[2]Finnish Meteorological Institute, 00101, Helsinki, Finland
[3]Research Infrastructure Services, Natural Resources Institute Finland, 00791 Helsinki, Finland
[4]Helsinki Institute of Sustainability Science, Faculty of Science, 00014, University of Helsinki, Finland

Correspondence: Sasu Karttunen (sasu.karttunen@helsinki.fi)

Abstract. The structure of the urban boundary layer, and particularly the surface layer, displays significant complexity, which can be exacerbated by coastal effects for cities located in coastal regions. Resolving the complexity of the coastal urban boundary layer remains an important question for many applications such as air quality and numerical weather prediction. One of the most promising new techniques for measuring the structure of the surface layer is fibre-optic distributed temperature sensing (DTS), which has the potential to provide new significant insights for boundary layer meteorology by making it possible to study thermal turbulence with high spatial and temporal resolution.

We present 14 weeks of profile measurements with a DTS system at an urban site in Helsinki, Finland, during the winter and spring of 2020. We assess the benefits and drawbacks of using DTS measurements to supplement sonic anemometry for longer measurement periods in varying meteorological conditions, including those found difficult for the DTS method in prior studies. Furthermore, we demonstrate the capabilities of the DTS system using two case scenarios: a study of the erosion of a near-ground cold layer during the passage of a warm front, and a comparison of the near-ground thermal structure with and without the presence of a sea-breeze cell during springtime convective boundary layer development.

This study demonstrates the utility of DTS measurements in revealing the internal surface layer structure, beyond the predictions of traditional surface layer theories. This knowledge is important for improving surface layer theories and parametrisations, including those used in numerical weather prediction. The study also highlights the drawbacks of DTS measurements, caused by low signal-to-noise ratios in near-neutral atmospheric conditions, especially when such a system would be used to supplement turbulence measurements over longer periods. Overall, this study presents important considerations for planning new studies or ongoing measurements utilising this exciting and relatively new instrumentation.

https://doi.org/10.5194/amt-2021-428
Preprint. Discussion started: 14 February 2022

Atmospheric Measurement Techniques Discussions

1 Introduction

The atmospheric boundary layer (ABL) is a dynamically and structurally complex layer directly influenced by the surface characteristics of the Earth and which controls the interaction between the surface and the atmosphere. Due to the turbulent nature of the ABL, it has remained notoriously difficult to study and theoretically describe. This applies especially to the urban boundary layer (UBL), a subtype of the ABL, where human influence has a high impact with surface characteristics heavily modified compared to natural surfaces (Barlow, 2014). The vertical structure of the UBL is strongly influenced by an increase in the surface roughness due to buildings and other structures, and the additional anthropogenic heating coming from sources such as buildings and traffic. The UBL can be considered to be an internal boundary layer (IBL) forming in conjunction with surrounding surfaces with different surface characteristics. This is especially the case where there are sharp borders between different surface types, such as coastal urban areas. The presence of an IBL causes spatial generalisation loss for point-like in situ measurements, as they represent only the specific IBL that the measurement instrument is located within.

In the lowest part of the UBL the flow and turbulence are strongly influenced by the surface. This layer is the roughness sublayer (RSL) and in some situations it can be deep enough that it extends up to the surface layer top, preventing an inertial sub-layer (ISL) from forming (Rotach, 1999; Cheng et al., 2007). Instruments for measuring the ABL structure are commonly installed within the ISL in order for them to be representative for the urban surface. Understanding the structure of the RSL and possible ISL above are fundamental for several meteorological applications such as pollutant transport and wind conditions.

A vast number of in situ and remote sensing observational methods have been utilised in ABL research over the years. Since the 1990s and early 2000s, sonic anemometers have formed the modern in situ backbone of micrometeorological studies (Aubinet et al., 2012). Sonic anemometers, by their capability of providing both the three-dimensional wind components and sonic temperature at high frequency, are particularly suited to providing surface fluxes using the eddy covariance (EC) method. However, sonic anemometry, like other point-like in situ methods, lack the desired spatial coverage unless multiple instruments are deployed. Deploying multiple instruments increases however the total cost of the system and thus have been rarely applied. Additionally, especially for horizontal setups, flow distortion by the instrumentation and their supporting structures adds a limit to the number of instruments that can be reasonably used. Therefore, methods that can provide better spatial and vertical coverage with fewer instruments and with less supporting structures can prove highly beneficial for ABL studies (Foken, 2017). This is especially true for RSL studies, where the inhomogeneous nature of turbulence requires detailed spatial coverage.

One increasingly utilised approach to provide three-dimensional spatial coverage of the ABL is to use ground-based remote sensing methods. Ceilometers provide information on the evolution of the boundary layer structure (Kotthaus et al., 2020) whereas scanning Doppler lidar can provide the wind profile (Päschke et al., 2015) and the turbulence structure (Manninen et al., 2018) in addition to the ABL depth (Tucker et al., 2009). These techniques provide great value for ABL studies but they commonly lack information on the RSL due to limitations in their resolution and the lowest altitude from which measurements are possible (Emeis, 2011). Other remote sensing instruments utilised in urban ABL studies include sodar (Bradley et al., 2015) and scintillometers (Ward, 2017), however, finding appropriate location in urban areas can be challenging.

https://doi.org/10.5194/amt-2021-428
Preprint. Discussion started: 14 February 2022


Atmospheric Measurement Techniques Discussions

One of the most promising new techniques for measuring the structure of the ABL is fibre-optic distributed temperature sensing (DTS) (eg. Selker et al., 2006; Tyler et al., 2009; Thomas et al., 2011). In a DTS system, laser pulses of a specific wavelength are sent from an instrument through an optical fibre. Some of this light is scattered within the fibre due to imperfections, but also due to the non-crystalline structure of glass. This scatter is composed of Rayleigh, Brillouin and Raman scatter. Raman backscattering is when the material (here the fibre) absorbs and then remits photons at a different wavelength to the transmitted wavelength; Stokes scattering refers to photons emitted at longer wavelengths, and anti-Stokes scattering refers to photons emitted at shorter wavelengths. The intensity of anti-Stokes scattering depends on temperature, whereas Stokes scattering is independent of temperature. Through this temperature dependency of the anti-Stokes signal, it is possible to derive the temperature of the fibre at high frequency, and provide along-fibre resolution using time-of-flight with the very short laser pulses (Selker et al., 2006).

DTS has already been used in a growing number of studies of the surface layer, including one-dimensional profile measurements of temperature (Keller et al., 2011; Higgins et al., 2018; Fritz et al., 2021; Peltola et al., 2021) and studies with two- or three-dimensional arrays (Thomas et al., 2011; Zeeman et al., 2015; Pfister et al., 2017, 2019; Mahrt et al., 2020). Furthermore, by usage of heated or wetted cables, DTS can be used to study wind speed (Sayde et al., 2015) or humidity (Schilperoort et al., 2018; Izett et al., 2019). However, most studies up to now span only a few days or a few weeks at maximum, and have generally focused on specific research questions well-suited for the technique. The performance of the DTS method for longer campaigns or continuous measurements has not been previously assessed. Various meteorological conditions can be challenging for DTS, as the method requires a relatively high amount of thermal turbulence to provide reliable estimates of thermal turbulence statistics (Peltola et al., 2021). Solar radiation can also induce an error in the measurements (De Jong et al., 2015), as does wetting of the cable due to precipitation or fog (Izett et al., 2019). These hinder the possibilities of DTS for supplementing, for example, eddy covariance (EC) instrumentation. Therefore, it is important to study the behaviour and performance of the method to better understand the suitability for supplementing further ABL studies.

This article presents an overview of 14 weeks of profile measurements with a DTS system at an urban site in Helsinki during the winter and spring of 2020. The main aims are to assess the benefits and drawbacks of DTS measurements for longer measurement periods in varying meteorological conditions, and demonstrate the usefulness of temperature profile measurements with DTS in a coastal surface layer beyond traditional turbulence statistics estimation using two case studies. The first case study investigates the erosion of a near-ground cold layer during the passage of a warm front. The second case study compares the near-ground thermal structure with and without the presence of a sea-breeze cell during springtime convective boundary layer (CBL) development. We demonstrate multiple ways of extracting useful information from the DTS measurements in varying environmental conditions, including those which could be described as challenging for the instrumentation used.

https://doi.org/10.5194/amt-2021-428
Preprint. Discussion started: 14 February 2022

Atmospheric Measurement Techniques Discussions

2 Materials and methods

2.1 Measurements

2.1.1 Measurement site

The DTS measurement campaign was conducted at the SMEAR III Kumpula station (Järvi et al., 2009), located in Helsinki, Finland, approximately $4\ \mathrm{km}$ north-east from the city centre ($60.203°$ N, $24.961°$ E) from 25 January to 5 May 2020. The majority of the inner city is located on a $7\ \mathrm{km}$ long north-south oriented peninsula on the northern coastline of the Gulf of Finland. The peninsula is surrounded by two narrow bays to the east and west, with the minimum distance from the measurement site to the eastern bay being approximately $1\ \mathrm{km}$.

The measurement site is on top of a 27-metre hill (Fig. 1), $29\ \mathrm{m}$ above sea level (ASL). The site is separated from dense urban development in the south-west by a 500-metre wide valley with the bottom at $2\ \mathrm{m}$ ASL. To the east the terrain slopes towards the sea, with the steepest gradient next to the measurement site. On top of the hill, immediately to the north-north-west from the measurement site, are buildings with rooftop heights between 9 and 24 metres. The slopes of the hill are mainly covered with deciduous broad-leaved trees in all directions, with canopy tops reaching up to $40\ \mathrm{m}$ ASL north-west, $33\ \mathrm{m}$ ASL west to south, and $35\ \mathrm{m}$ ASL east to north-east of the measurement site. The measurements took place during the leaf-free season.

Overall, the distinctive upwind features around the site can be labelled based on wind direction (WD) as follows (Vesala et al., 2008):

$$\text{Sector} = \begin{cases} \text{Campus buildings}, & 320° \leq \text{WD} < 40°, \\ \text{Main road}, & 40° \leq \text{WD} < 180°, \\ \text{Vegetation}, & 180° \leq \text{WD} < 320°. \end{cases} \quad (1)$$

2.1.2 DTS instrumentation

The DTS system consisted of an optical fibre installed vertically on a 31 metre high measurement mast. The measurement instrument (ULTIMA-S, 0–5 km variant; Silixa Ltd, Hertfordshire, UK) was located in an air-conditioned equipment container next to the mast. 50 l cooler tanks were filled with water and used as calibration baths, as in Peltola et al. (2021). One bath was located outside the container and hence the bath water temperature followed the ambient temperature slowly, whereas the other bath was inside the container and the bath water temperature remained at the indoor temperature (around 26 °C). Given the timing of the measurement campaign (winter, early spring), the temperature difference between the baths was adequate for DTS calibration. The water temperatures were monitored with PT100 sensors (supplied and logged with the instrument at 0.01°C precision) to provide reference temperatures for post-calibration. Both baths were equipped with an aquarium pump to prevent stratification of the water through continuous mixing.

An aramid-reinforced $50\ \mu\mathrm{m}$ multimode fibreoptic cable (AFL Telecommunications LLC, Duncan, SC 29334, US) was used for the measurements. The total length of the cable was approximately 198 metres. A small diameter white coated fibre was

https://doi.org/10.5194/amt-2021-428
Preprint. Discussion started: 14 February 2022

Atmospheric Measurement Techniques Discussions

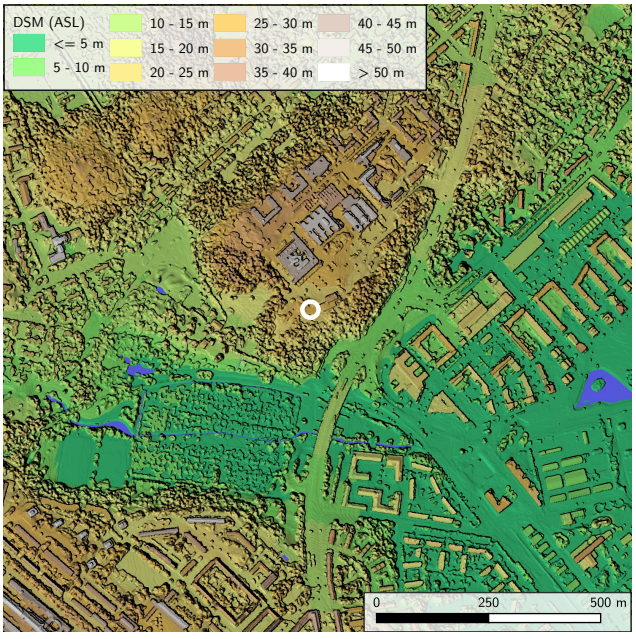

Figure 1. A hill-shaded digital surface model (including vegetation) of the measurement site and surroundings. The mast location is marked with a white circle. The underlying lidar-derived digital surface model is provided by the City of Helsinki (2017) (CC-BY 4.0).

selected in order to minimise the impact of shortwave radiation exposure, which can potentially have a significant effect on DTS measurements (De Jong et al., 2015). This may be especially important in urban environments, where buildings and other structures can cast hard shadows on the fibre. The fibre was installed to run out of the instrument, through both calibration baths, up and down the mast, again through the calibration baths and back to the instrument allowing reference measurements at both the beginning and end of the cable. The fibre extending from 1.8 to 29 m above ground level (AGL) was attached to the SW side of the mast at five points, with approximately one metre horizontal separation from the mast. Despite careful mounting of the fibre, the connection points caused disturbances in the data, and consequently, data points close to the connection points were removed from subsequent analysis. The measurement setup provided a double measurement of the vertical profile of air temperature at 12.7 cm spatial and 1 Hz temporal resolution. In double-ended mode, each direction along the cable was measured sequentially, so that the temperature data at the end were available at 0.5 Hz resolution.

A total of 2202 hours of DTS data were recorded over the period of the measurement campaign, covering approximately 90 % of the whole period. The longest measurement break was from 18 March 17:30 UTC to 25 March 12:00 UTC. Three shorter breaks occurred in February: 4 February 13:30 UTC to 6 February 00:00 UTC; 11 February from 01:00 UTC to midnight; and 25 February from 09:00 UTC to midnight. All of these data gaps were due to data transfer issues not related to the instrument itself.

https://doi.org/10.5194/amt-2021-428
Preprint. Discussion started: 14 February 2022


Atmospheric Measurement Techniques Discussions

2.1.3 Supporting instrumentation

The measurement mast on which the DTS system was installed features continuous eddy covariance (EC) measurements and auxiliary meteorological measurements. These measurements are part of the ICOS (Integrated Carbon Observation System) research infrastructure. The EC measurement system uses an ultrasonic anemometer (USA-1, Metek GmbH, Germany) to measure 3-D orthogonal wind speed components (u, v, and w) and the sonic temperature (T_s) at a 10 Hz sampling rate. The anemometer is located at the top of the 31-metre (60 m ASL) mast.

The data from the anemometer were used in this study as a reference for the DTS-derived temperature statistics as well as for mean wind speed and direction. Measurements from a 4-component net radiometer (Huskeflux NR01, Hukseflux Thermal Sensors B.V, The Netherlands) were used to estimate the global radiation exposure. The radiometer is located at the mast top and is sampled at one minute intervals. Humidity and 2-metre temperature observations from Vaisala HMP 155D (Vaisala Oyj, Finland) probe used at an official weather station located at the site were used, as well as precipitation accumulation measured using an OTT Pluvio2 raingauge (OTT Hydromet GmbH, Germany).

2.2 Data post-processing

The DTS measurements were post-calibrated using the double-ended calibration method described in detail by de Giesen et al. (2012). First, the raw temperature signal was determined from the ratio of the Stokes and anti-Stokes backscatter using the equation (Farahani and Gogolla, 1999; Hausner et al., 2011)

$$T(x,t) = \frac{\gamma}{\ln\left(\frac{P_s(x,t)}{P_{as}(x,t)}\right) + C(t) + \int_0^x \delta\alpha(x')dx'}, \tag{2}$$

where T is the post-calibration temperature, γ is a calibration constant, x distance from the instrument along the fibre, $P_s(x,t)/P_{as}(x,t)$ the ratio of the Stokes and anti-Stokes backscatter received at the instrument, $C(t)$ is a time-dependent calibration function and the last term in the denominator represents the cumulative differential attenuation computed separately for each 30-min averaging period. γ and $C(t)$ were determined in a two-step process described by Peltola et al. (2021): 1) both $C(t)$ and γ were fitted as time-dependent variables, and 2) $C(t)$ was re-fitted while γ was fixed to a constant value equal to the mean of the γ values from the first step. In order to reduce the noise, the two simultaneous T profiles (up and down) were averaged prior to analysis. Furthermore, the potential temperature θ used in the analysis was computed from T by reducing them to the mast base height using the standard dry lapse rate.

Two datasets, one containing 30-min turbulence statistics and one containing denoised high frequency data, were computed post-calibration. 30-min turbulence statistics were derived using the methodology described by Lenschow et al. (2000) following Peltola et al. (2021). Prior to estimating the statistics the DTS data were averaged vertically over 0.5 m distance in order to further reduce the noise. After Reynolds averaging, the fluctuating part of the raw DTS-estimated T signal (T'_{raw}) can be written as a combination of the true signal $T'(t)$ and time-dependent instrument noise $\epsilon(t)$ as $T'_{raw} = T' + \epsilon$. The second-order autocovariance of the signal can be then written as

$$M_{11}(t_1) = \overline{(T' + \epsilon)(T'_1 + \epsilon_1)}, \tag{3}$$

https://doi.org/10.5194/amt-2021-428
Preprint. Discussion started: 14 February 2022


Atmospheric Measurement Techniques Discussions

where the overline denotes a temporal average and the subscript 1 lag-t_1 time series. Given that T' and ϵ are uncorrelated, it can be shown that

$$M_{11}(0) = \overline{T'^2} + \overline{\epsilon^2}. \tag{4}$$

Assuming uncorrelated noise, the true signal variance $\overline{T'^2}$ and the square of instrument noise variance $\overline{\epsilon^2}$ can be estimated by extrapolating the autocovariance function to lag zero

$$\sigma_T^2 = \overline{T'^2} = M_{11}\left(t_1 \to 0\right) \tag{5}$$

$$\overline{\epsilon^2} = M_{11}\left(0\right) - M_{11}\left(t_1 \to 0\right). \tag{6}$$

For third-order moments, a third-order autocovariance function (M_{21}) can be used similarly

$$\overline{T'^3} = M_{21}\left(t_1 \to 0\right) \tag{7}$$

$$\overline{\epsilon^3} = M_{21}\left(0\right) - M_{21}\left(t_1 \to 0\right). \tag{8}$$

The signal-to-noise ratio (SNR) was computed from the second order statistics

$$\mathrm{SNR} = \frac{\sigma_T^2}{\overline{\epsilon^2}}. \tag{9}$$

To assess the comparability of DTS-estimated higher order statistics against those estimated from the EC system, the absolute differences between DTS and EC 30-minute variance and skewness estimates were computed. For variance, the absolute difference scaled to unit variance

$$D_{\sigma_\theta^2} = \frac{\left|\sigma_{\theta_{\mathrm{EC}}}^2 - \sigma_{\theta_{\mathrm{DTS}}}^2\right|}{\sigma_{\theta_{\mathrm{DTS}}}^2} \tag{10}$$

and for skewness the absolute difference of Pearson's moment coefficients of skewness (S_θ)

$$D_{S_\theta} = \left|S_{\theta_{\mathrm{EC}}} - S_{\theta_{\mathrm{DTS}}}\right| \tag{11}$$

were used as a difference metric. The highest measurement height in the post-prosessed dataset (28.64 m) was used in the comparison. The height separation between the DTS measurement point and the sonic anemometer (31 m) causes a small systematic error in the observed differences between the two measurement methods, but the size of this systematic error was qualitatively assumed to be small enough to be ignored in this study. Furthermore, the root-mean-square-difference (RMSD) and 95th percentile range were computed for the deviations for ten equally sized data bins sorted and allocated based on SNR, in order to find a level of SNR above which the DTS estimates are reliable enough.

https://doi.org/10.5194/amt-2021-428
Preprint. Discussion started: 14 February 2022


Atmospheric Measurement Techniques Discussions

The high frequency dataset was constructed by de-noising the calibrated raw temperature signal using a singular value decomposition (SVD) -based de-noising methodology, similar to that used by Epps and Krivitzky (2019). SVD of a data matrix $\mathbf{T} \in \Re^{n \times m}$ is

$$\mathbf{T} = \sum_{i=1}^{n} \mathbf{u}_k \, s_k \, \mathbf{v}_k^{\top}, \tag{12}$$

where $\mathbf{u}_k$ is the left singular vector, s_k is a singular value and $\mathbf{v}_k$ is the right singular vector of the kth SVD mode. s_k^2 corresponds to the variance of the data matrix at the kth SVD mode and hence the overall variance of the data can be estimated from the sum of all s_k^2 values. Following Epps and Krivitzky (2019), it was assumed that at high i, the SVD modes were dominated by noise and hence s_k at high i follows the Marchenko-Pastur distribution (see Epps and Krivitzky, 2019, for details). Based on this the clean (i.e. noise-free) singular values ($\tilde{s}_k$) were reconstructed as

$$\tilde{s}_k = \begin{cases} \sqrt{s_k^2 - s_{noise,k}^2}, & k < k_c \\ 0, & k \geq k_c \end{cases},$$

where $s_{noise,k}^2$ represent the noise variance at the kth SVD mode estimated based on the Marchenko-Pastur distribution and k_c is the minimum index k for which $s_k > s_{noise,k}$. Then the de-noised data matrix $\tilde{\mathbf{T}}$ was reconstructed via

$$\tilde{\mathbf{T}} = \sum_{i=1}^{n} \mathbf{u}_k \, \tilde{s}_k \, \mathbf{v}_k^{\top}. \tag{13}$$

Note that here the reconstruction was performed using all SVD modes and $\tilde{s}_k$, not just the few lowest modes as in Epps and Krivitzky (2019). The de-noising algorithm described above was applied to the temperature profiles using 30-min blocks. The strength of the SVD-based de-noising over de-noising using, for example, wavelets is that SVD is fully data-driven, meaning that it is not necessary to find a suitable mother wavelet for the dataset in question.

The turbulent statistics and fluxes were computed from the EC data using commonly accepted procedures following Aubinet et al. (1999), with a data post-processing pipeline used at the site as described in Nordbo et al. (2013). Flux stationary screening using the 0.3 limit had the most significant effect on EC data availability, reducing the total EC data availability over the measurement period from 2401 hours to 1559 hours.

2.3 Theoretical vertical profiles of potential temperature and its variance in the surface layer

The Monin-Obukhov similarity theory (MOST) can be used to predict 1D-profiles of scaled mean and turbulent quantities within the surface layer. Whilst it is well-known that the assumptions used in MOST are not valid in the RSL (Rotach, 1999; Barlow, 2014), which can cover a large portion of the surface layer of the UBL, it is nevertheless a widely used theoretical reference for lower boundary layer profile studies. MOST predicts that the mean and turbulence profiles can be parametrised as unique functions of the stability parameter (Monin and Obukhov, 1954):

$$\zeta = z/L, \tag{14}$$

https://doi.org/10.5194/amt-2021-428
Preprint. Discussion started: 14 February 2022


Atmospheric Measurement Techniques Discussions

where z is the effective measurement height (measurement height reduced by possible displacement height) and L is the Obukhov length defined as

$$L = \frac{-u_*^3 \overline{\theta}}{kg\overline{w'\theta'}}, \tag{15}$$

where u_* is the friction velocity, $\overline{\theta}$ is the mean potential temperature, k is von Kármán's constant, g is the gravitational acceleration and $\overline{w'\theta'}$ is the kinematic heat flux.

Using the surface layer temperature scale

$$\theta_* = -\frac{\overline{w'\theta'}}{u_*}, \tag{16}$$

the surface layer temperature gradient can be parametrised as a function of ζ:

$$\frac{\partial \overline{\theta}}{\partial z} = \frac{\theta_*}{kz}\phi_\theta(\zeta), \tag{17}$$

where ϕ_θ is a similarity function for mean temperature. The temperature profile in the surface layer can then be obtained by integration:

$$\overline{\theta}(z_2) - \overline{\theta}(z_1) = \frac{T_*}{k}\int_{z_1}^{z_2} \frac{1}{z}\phi_\theta(\zeta)\,\partial z. \tag{18}$$

Various forms of ϕ_θ have been proposed over the years, with the so-called Businger-Dyer form (Businger, 1988)

$$\begin{aligned} &\phi_\theta(\zeta) = 1 + C_1\zeta, \quad \text{when } \zeta > 0 \\ &\phi_\theta(\zeta) = (1 - C_2\zeta)^{-1/2}, \quad \text{when } \zeta < 0, \end{aligned} \tag{19}$$

where constants C_1 and C_2 are to be determined empirically, being one of the most commonly used.

Instead of the detailed temperature profile described by Eq. 18, it is often enough and useful to describe the overall stratification within an air column between z_1 and z_2 using a single measure. For this, column-integrated buoyancy B (Lareau and Horel, 2015)

$$B = g\int_{z_1}^{z_2} \left[\frac{\theta_{z_1} - \theta_{z_2}}{\theta_{z_1}}\right] \partial z \tag{20}$$

can be used. As the name suggests, this represents the integrated buoyant force across the defined column. MOST-predicted B can be estimated and subsequently compared to the observed B by further integrating Eq. (18) as above.

Similarly to mean quantities, the integral turbulence characteristics (ITC), i.e. the standard deviations of turbulent variables normalised using their respective scaling, can be parametrised using MOST. Using the surface layer temperature scale θ_* we can write the parametrisation for the standard deviation of potential temperature as (Panofsky et al., 1977)

$$\frac{\sigma_\theta}{\theta_*} = \phi_{\sigma_\theta}(\zeta), \tag{21}$$

https://doi.org/10.5194/amt-2021-428
Preprint. Discussion started: 14 February 2022


Atmospheric Measurement Techniques Discussions

where ϕ_{σ_θ} is a similarity function for temperature ITC. A widely suggested form for ϕ_{σ_θ} in unstable conditions is (eg. Panofsky et al., 1977; J. C. and J. J., 1994; Liu et al., 1998; Andreas et al., 1998; Wilson, 2008)

$$\phi_{\sigma_\theta}(\zeta) = C_1 (1 - C_2\zeta)^{C_3}, \tag{22}$$

with constants C_1, C_2 and C_3 to be determined empirically. A recent large eddy simulation based study by Maronga and Reuder (2017) found values of $C_1 = -2.1$, $C_2 = 9$ for $C_3 = -1/3$, which is the power traditionally used in the literature. These values produce similar results to the sonic anemometer measurement based studies by Andreas et al. (1998) and Liu et al. (1998), who found values of $C_1 = -2.0$, $C_2 = 8$ and $C_1 = -3.2$, $C_2 = 28.4$ respectively. Maronga and Reuder also suggested a slightly different shape for the similarity function with $C_3 = -0.4$ based on the simulation data, but due to the lack of measurement-based evidence, we used the values for the traditional $C_3 = -1/3$ form suggested by the study.

Assuming the validity of MOST and vertically-constant fluxes, θ_* and L are expected to be near constant in the surface layer, and Eqs. (21) and (22) can be used to predict profiles of $\overline{\theta}$ and σ_θ respectively using EC measurements only from one level. In reality, the presence of a constant flux layer depends on how developed the flow is, which itself depends on upwind surface heterogeneities, large-scale atmospheric forcing (e.g. Rotach, 1999). Additionally, closer to the ground, namely in the roughness sublayer, local heterogeneity of the flow breaks the assumptions of a constant flux layer and subsequently those of MOST. Thus, observed profiles of ITCs are expected to deviate from those predicted using MOST in the lower portions of the surface layer.

2.4 Wavelet analysis

To study the spectro-temporal properties of the measured time series, we utilise the continuous wavelet transform (CWT). In CWT, as for wavelet transforms (WT) in general, a wavelet function is used to unfold a signal into time-frequency space.

CWT of a finite discrete signal of a turbulent quantity $q(t_m)$ with an uniform time step δt is obtained by convolving it with a scaled and translated analysing wavelet $\Psi(\eta_m)$. After normalisation to unit energy, this can be written as

$$W_q(s, t_n) = \left(\frac{\delta t}{s}\right)^{1/2} \sum_{m=0}^{N} q(t_m) \Psi_0^*(\eta_m)\, \delta t, \tag{23}$$

where $\eta_m = (t_m - t_n)/s$, $\Psi_0^*(\eta_m)$ is the complex conjugate of $\Psi(\eta_m)$ normalised to unit energy and $(\delta t/s)^{1/2}$ is a scaling factor. By altering the wavelet scale s and translating along the localised time index t_n, one can evaluate the function $W_q(s, t_n)$ on a time-scale plane, producing a scalogram. The finite bounds used in Eq. (23) induce significant edge effects when the wavelet's cone of influence, i.e. e-folding time of $\Psi(\eta_m)$, extends beyond the bounds of the original time series (Torrence and Compo, 1998).

Although the selection of scales to be used for CWT can be theoretically arbitrary, for reconstruction purposes it is convenient to construct the scales as fractional powers of two (Torrence and Compo, 1998):

$$s_j = s_0 2^{j\delta j}, \text{ for } j = 0,\ 1,\ ...,\ J, \tag{24}$$

https://doi.org/10.5194/amt-2021-428
Preprint. Discussion started: 14 February 2022


Atmospheric Measurement Techniques Discussions

where s_0 is the smallest resolvable scale, δj is the spacing factor and J is the number of scales plus one. To include scales up to the largest scale possible given the length of the time series, one can select $J = \delta_j^{-1} \log_2 (N\delta t / s_0)$.

Following bias rectification proposed by Liu et al. (2007), the discrete wavelet power of the signal can be computed from the normalized transform as the square of the norm of the transform divided by the associated scale: $|W_q(s_j, t_n)|^2 / s_j$. From this, the global discrete wavelet variance spectrum can be reconstructed as

$$E_q(s_j) = \frac{\delta j \delta t}{C_\delta} \frac{1}{N} \sum_{n=0}^{N} \frac{|W_q(s_j, t_n)|^2}{s_j}, \tag{25}$$

where C_δ is a wavelet-specific reconstruction factor. E_q is defined here in such a way that an estimate of the global variance of the time series can be reconstructed as the sum of $E_q(s_j)$ over all s_j defined in Eq. (24):

$$\sigma_q^2 = \sum_{j=0}^{J} E_q(s_j), \tag{26}$$

analogous to the Fourier discrete variance spectrum described in Stull (1988). The accuracy of this variance estimate depends on the spacing factor δj used and the analysing wavelet (Schaller et al., 2017). Similarly, a local variance estimate can be reconstructed as

$$\sigma_q^2(t_n) = \frac{\delta j \delta t}{C_\delta} \sum_{j=0}^{J} \frac{|W_q(s_j, t_n)|^2}{s_j}, \tag{27}$$

producing a temporally localised variance estimate with a time resolution of δt. Although localised in time, this estimate includes variance contributions from all scales represented by s_j, and is thus well suited to studying non-stationary conditions and short-time events, as no steady-state assumption is required (Schaller et al., 2017). By limiting the s_j range included in the sum, band-passed localised variance estimates can be obtained.

The selection of a wavelet depends on multiple factors, which are discussed in detail for example in Farge (1992) and Torrence and Compo (1998). For our case, we selected the Morlet wavelet, a non-orthogonal complex wavelet which provides a good relative balance between time and frequency localisation (e.g. Baars et al., 2015). Formally the Morlet wavelet is a complex-valued plane wave carrier in a Gaussian envelope (Farge, 1992)

$$\Psi_0(\eta) = \pi^{-1/4} e^{i\omega_0 \eta} e^{-\eta^2/2}, \tag{28}$$

where ω_0 is a non-dimensional frequency and subscript zero in Ψ_0 indicates that the wavelet is normalised to unit energy. By varying ω_0, the relative balance between time and scale localisation can be altered. A value of $\omega_0 = 6$ is commonly used. For the Morlet wavelet, the equivalent Fourier wavelength λ of a given wavelet scale can be computed from the relation (Torrence and Compo, 1998)

$$\lambda = \frac{4\pi s}{\omega_0 + \sqrt{2 + \omega_0^2}}. \tag{29}$$

Subsequently, the spectral energy density can be estimated with the help of Eq. (25) as

$$S_q = \frac{E_q(s_j)}{\Delta f(s_j)}, \tag{30}$$

https://doi.org/10.5194/amt-2021-428
Preprint. Discussion started: 14 February 2022


Atmospheric Measurement Techniques Discussions

where $f(s_j)$ is the Fourier frequency corresponding to s_j.

3 Results and discussion

3.1 Data quality and conditional sampling

To evaluate the influence of shortwave radiation exposure on the fibre, deviations of the DTS-estimated 30-min 2-metre average potential temperature $\overline{\theta}_{DTS}$ from the 2-metre reference temperature were studied as a function of mean global radiation $\overline{Q}$ (Fig. 2a). On average, the deviations show a near-zero dependency on $\overline{Q}$, with a least squares linear fit slope of $\beta_1 = 6.4 \times 10^{-5}\mathrm{K\ W^{-1}\ m^2}$. The overall root-mean-square-error (RMSE) for $\overline{\theta}_{DTS}$ is 0.23 K, 23 times the reported temperature resolution of the DTS sensor (0.01 K). The radiation-induced error is significantly smaller than reported for a white fibre by De Jong et al. (2015) (0.61 K), potentially due to the smaller outer diameter of the fibre used (0.9 mm vs. 1.6 mm here). Moreover, De Jong et al. (2015) had their cables aligned horizontally whereas in our measurement setup the cables were aligned to the vertical which should result in less radiation per unit of cable surface. As the fibre is unprotected from precipitation, evaporative cooling of precipitation-wetted fibre causes the DTS system to measure wet bulb temperature instead of air temperature. This is highlighted in Fig. 2b: the 30-min periods with accumulated liquid-phase precipitation of $P \geq 0.1$ mm show a negative bias compared to the reference, whereas the remaining data do not show such a bias. This is expected, as wet bulb temperature is always less than or equal to the air temperature, and equal only in water vapour saturated air. This also explains the relatively high number of data points with negative deviations close to $\overline{Q} = 0\ \mathrm{Wm^{-2}}$ in Fig. 2a. This highlights the usefulness of accompanying DTS measurements with precipitation and humidity measurements, and the importance of knowing the meteorological conditions when analysing DTS measurements. The remaining deviations not explained by precipitation or shortwave exposure may yield from multiple sources, including horizontal separation between the sensors and longwave radiative cooling of the cable at night.

The comparisons of the DTS-estimated higher order statistics against those estimated from the EC system (Fig. 3) reveal a divergence in estimates between the two measurement techniques as SNR approaches zero. This is caused by two factors. The accuracy of the statistics estimation using the Lenschow method decreases with SNR and therefore, some conditional sampling based on SNR is required in order to improve the reliability of the estimates. For variance estimates, RMSD does not decrease with SNR past the fifth data bin centred at $\mathrm{SNR} = 0.26$, with the 95th percentile difference converging at the sixth data bin centred at $\mathrm{SNR} = 0.37$. However, the skewness RMSD decreases up to the seventh bin, centred at $\mathrm{SNR} = 0.55$, with the 95th percentile difference decreasing even up to the eighth bin. Determining a minimum acceptable level of SNR for which the estimation of turbulent quantities is still reasonable requires a subjective interpretation. We chose $\mathrm{SNR} = 0.5$ as a conservative threshold value, based on both the variance and skewness RMSD curves. The same threshold value was used by Peltola et al. (2021).

As the magnitude of the signal noise is nearly constant, SNR-based screening of the 30-min averaged dataset effectively results in conditional sampling biased towards conditions with higher temperature variance. Temperature fluctuations are generally produced by either thermal turbulence in unstable conditions or mechanically-induced turbulent mixing of a stably

https://doi.org/10.5194/amt-2021-428
Preprint. Discussion started: 14 February 2022

Atmospheric Measurement Techniques Discussions

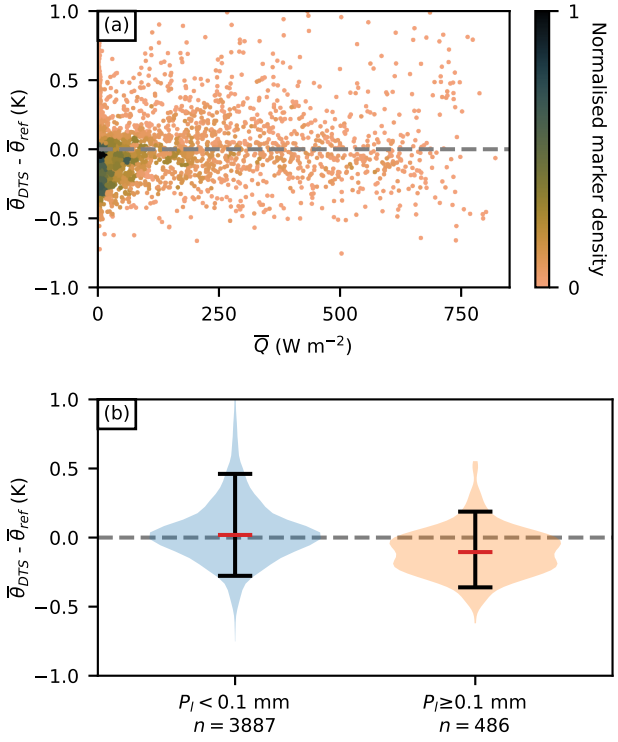

Figure 2. (a) Deviations of the DTS-estimated 30-min potential temperature ($\overline{\theta}_{DTS}$) from the corresponding mean reference potential temperature ($\overline{\theta}_{ref}$) measured at an official weather station next to the measurement mast as a function of global radiation $\overline{Q}$. The colour scale illustrates the relative marker density. (b) A violin plot of the same deviations for two groups of data: 30-minute accumulated liquid-phase precipitation $P_l < 0.1$ mm and $P_l \geq 0.1$ mm. Violin bodies represent the data distribution, black whiskers the 5th to 95th interpercentile range, and the red line the median.

stratified temperature profile, bringing gusts of warmer air aloft downwards. Neither of these are strong with low absolute values of ζ, corresponding to neutral or near-neutral conditions. Therefore, a significant portion of the data corresponding to these conditions are removed in SNR-based screening. This is clearly visible in the frequency distributions of EC-derived ζ after screening, as illustrated in Fig. 4. The ζ distribution corresponding to the filtered dataset is heavily biased towards unstable conditions. However, some of the more stable conditions are retained, likely due to mechanically.induced mixing across a stably-stratified profile causing temperature fluctuations.

In general, the measurement period in 2020 was stability-wise less variable than a 10-year reference period computed over the same days of year as the for the DTS measurement period. With few clear sky days with strong temperature inversions, near-neutral conditions prevailed, producing a more concentrated ζ distribution around zero compared to the reference period. As a consequence, screening with SNR $= 0.5$ results in only 42% of the 30-min averaging periods retained. Had the weather been more typical for the period, the percentage would probably been higher, as there would be more averaging periods with

https://doi.org/10.5194/amt-2021-428
Preprint. Discussion started: 14 February 2022

Atmospheric Measurement Techniques Discussions

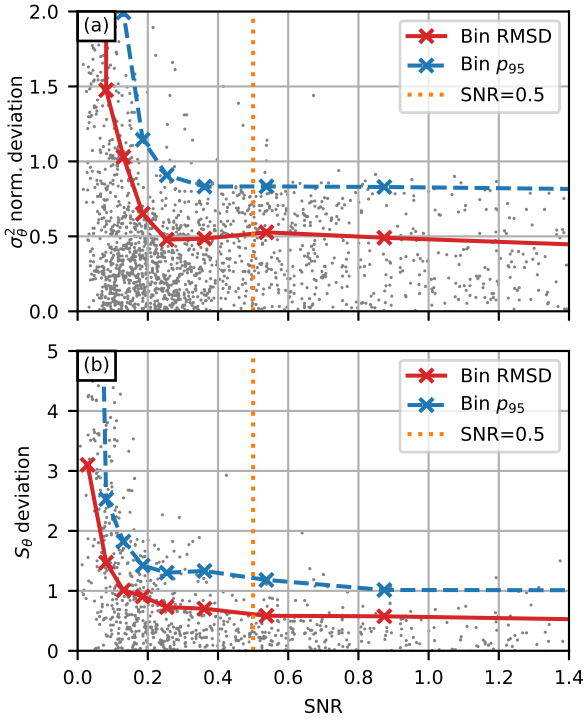

Figure 3. Deviations of the DTS-estimated temperature (a) variance and (b) skewness from the corresponding estimates using the sonic anemometer data. The red solid lines are the root-mean-square-deviations (RMSD) computed for 10 equally-sized bins (bin centres marked with x). The blue dashed lines are the corresponding 95th percentiles for each bin.

higher $|\zeta|$. The consequential bias towards higher $|\zeta|$ emphasises the relatively high sensitivity of the DTS system performance to meteorological conditions, which is important to keep in mind when planning DTS measurements.

When studying the portion of data retained as a function of height and time (Fig. 5), the role of solar radiation on generation of temperature fluctuations becomes evident. More data are retained in late spring, around midday, and closer to the ground when the occurrence of acceptable SNR values reach 60-80%. According to MOST, the temperature variance increases with decreasing height within the surface layer (Eq. 21), which in turn may cause SNR to cross the threshold value mid-profile in certain conditions. As expected, SNR shows a clear nocturnal cycle and an increasing trend over the whole measurement period. This emphasises that SNR-screened DTS-estimated statistics are not equally representative for all times of day and days of year.

3.2 Surface layer scaling

One of the main benefits of DTS is the potential for larger spatial coverage than with conventional techniques, such as sonic anemometers. In Fig. 6, the profiles of DTS-derived temperature ITCs for unstable conditions are compared to predictions

https://doi.org/10.5194/amt-2021-428
Preprint. Discussion started: 14 February 2022

Atmospheric Measurement Techniques Discussions

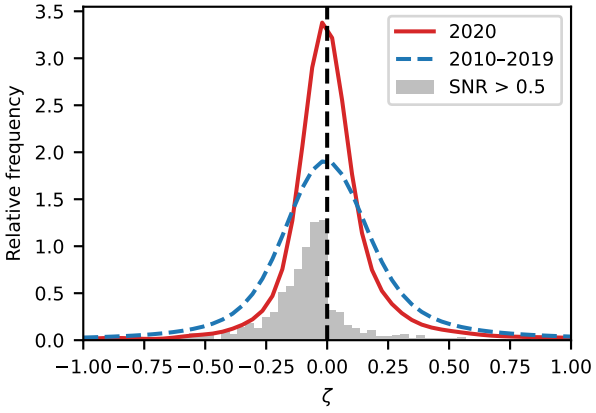

Figure 4. Relative frequency distributions of EC-derived 30-min stability parameter ζ for the DTS measurement period (red solid line), same after conditional sampling with SNR > 0.5 (grey bars), and for 10-year reference period including only the days of year within the DTS measurement period (blue dashed line). The continuous distributions are estimated from the EC data using kernel density estimation with a Gaussian kernel.

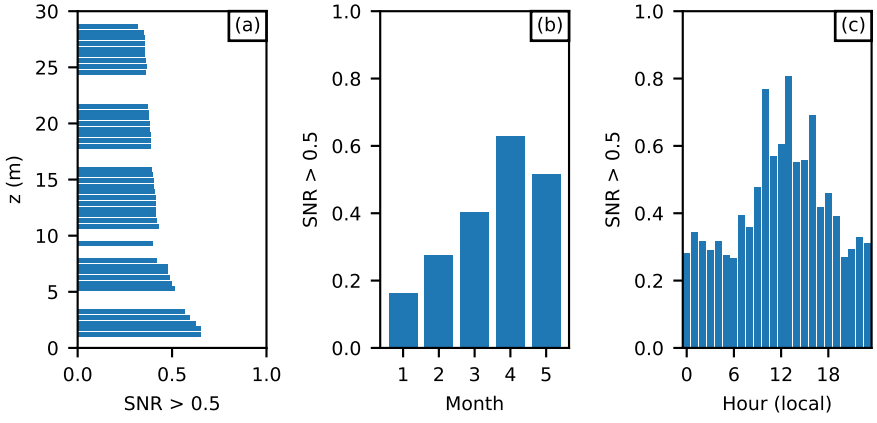

Figure 5. Fraction of data preserved fulfilling SNR > 0.5 threshold as (a) a function of height, (b) month and (c) hour of day in local time (EET/EEST). Note that January and May only contain data from five days.

from the similarity function in Eq. (22) and to those estimated from the EC measurements. The similarity functions converge to similar values in DTS and EC at the top of the mast, and are generally in good agreement with the DTS throughout the profile for very unstable conditions ($\zeta < -0.3$). For mildly unstable conditions ($-0.3 > \zeta > -0.05$) there is a considerably growing discrepancy between the profiles on moving down the profile towards the surface. This is not unexpected, since the lowest measurement levels are in the roughness sublayer in all wind directions, where MOST scaling is not expected to hold. For the main road wind sector especially, the deviation of the DTS profile from the similarity function is already considerable from

https://doi.org/10.5194/amt-2021-428
Preprint. Discussion started: 14 February 2022

Atmospheric Measurement Techniques Discussions

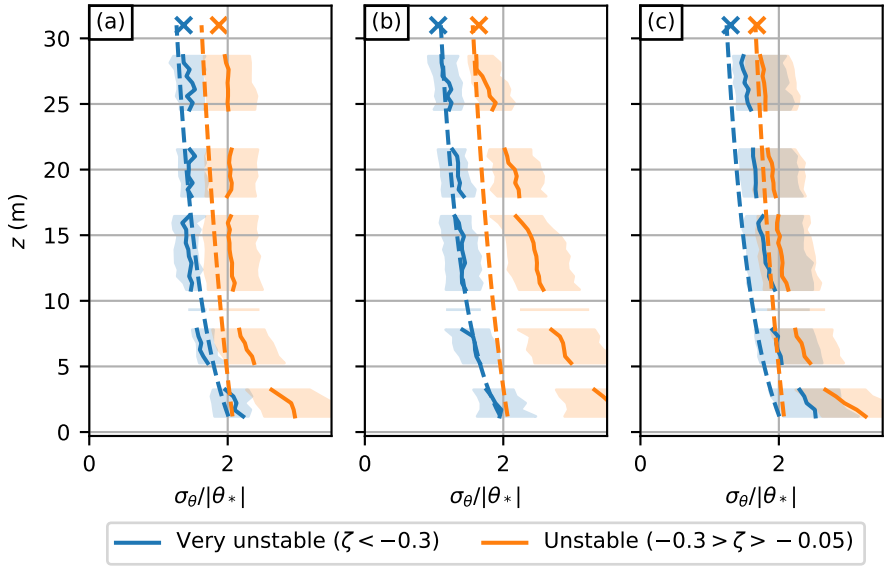

Figure 6. Median profiles of normalised temperature standard deviations (ITCs) in unstable conditions (solid lines) for three wind sectors: (a) campus buildings, (b) main road and (c) vegetation, with p_{25-75} inter-percentile range shaded. The corresponding estimates from the EC system are marked with "x" and reference similarity functions are drawn using dashed lines.

quite far up the profile. It is possible that the deviation is caused by upstream inhomogeneities in the surface properties. Given that the sea is approximately one-to-two kilometres away in the direction of the main road it is possible that in mildly unstable conditions there at least occasionally exists a thermal IBL with a height less than the mast top height. This would result in the observed median temperature ITC profile, which drastically exceeds that predicted by the MOST similarity relation for the lower sections of the mast.

It is to be emphasised that zero-plane displacement height was ignored when computing the similarity functions assuming minimal local displacement of the wind profile. As the mast is located on a hill top and the measurements were performed during the leaf-free season, the existence of a well-defined zero-plane displacement remains challenging. The DTS-estimated profiles do not show any clear discontinuity in shape. With a taller measurement mast, the DTS profiles could be used to obtain the displacement height by fitting a similarity function to the data with displacement height as the sole regressor. This could only be done if a significant stretch of the fibre was located clearly above the roughness sublayer; the current measurement mast is too short.

3.3 Warm front on 27 January 2020

Despite many averaged DTS datapoints having been filtered out by the SNR criteria, the high frequency data can still be used to study meteorological phenomena. To demonstrate the possibilities of using DTS data in low-SNR conditions, we studied

https://doi.org/10.5194/amt-2021-428
Preprint. Discussion started: 14 February 2022

Atmospheric Measurement Techniques Discussions

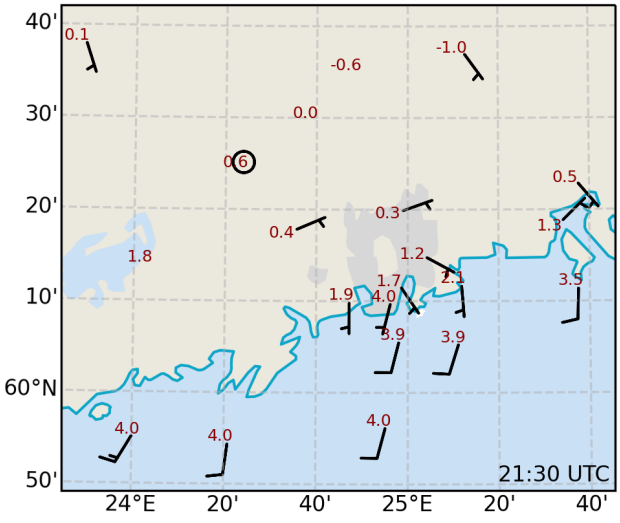

Figure 7. Surface observations of temperature and wind from official weather stations close to Helsinki on 27 January 2020 at 21:30 UTC.

measurements made during a passage of a warm front in closer detail. Late in the evening of 27 January 2020, a warm front associated with a North Atlantic low pressure system passed over Southern Finland and Helsinki eroded the near-ground cold layer beneath by downward mixing of the warm air aloft. Figure 7 presents the near-surface wind and temperature observations from nearby weather stations at the time the surface front reached the measurement site (21:30 UTC, 23:30 local). The west-northwest to east-southeast alignment of the front is visible as a strong surface temperature gradient and a turning of winds from SE to SW. Due to the inherently stable conditions and low wind speeds (1.7 to 3.3 ms^{-1}) during the passage of the front, the average SNR value was only 0.13 during this approximately one-hour event, significantly less than the $\mathrm{SNR} = 0.5$ threshold used in the quality screening for the 30-min averaged datasets. Furthermore, the nature of the event caused EC data to also be flagged during flux stationarity screening, emphasising the non-stationary nature of the event. From 16:00 to 23:20 UTC, 100% relative humidity was constantly observed at the official weather station, indicating very humid conditions.

Plotting the DTS-observed high frequency $\tilde{\theta}$ time series (Fig. 8a) reveals a turbulently progressing mixing process during the front passage. Warmer air aloft is mechanically entrained relatively slowly downwards, progressively increasing the temperatures along the profile. Time series of the column-integrated buoyancy (B) along the DTS profile (Fig. 8b) provide a more comprehensive overall picture of the thermal structure and propagation of the front. The average B starts to decrease from near-neutral at approximately 20:50 UTC, reaching $-0.57\ \mathrm{m}^2\ \mathrm{s}^{-2}$, and returns to near-neutral at 22:10 UTC. This demonstrates how, with the lack of thermal turbulence production in the stably stratified boundary layer, turbulence is generated through shear instability allowing entraining of warmer air aloft during the passage of the front. Inspecting the high frequency B time series reveals considerable deviations from the 10-min moving average, with peaks up to $-1.1\ \mathrm{m}^2\ \mathrm{s}^{-2}$. These deviations are of the same order as the mean value and one deviation causes the profile stability to return back to neutral briefly at 21:51 UTC.

https://doi.org/10.5194/amt-2021-428
Preprint. Discussion started: 14 February 2022

Atmospheric Measurement Techniques Discussions

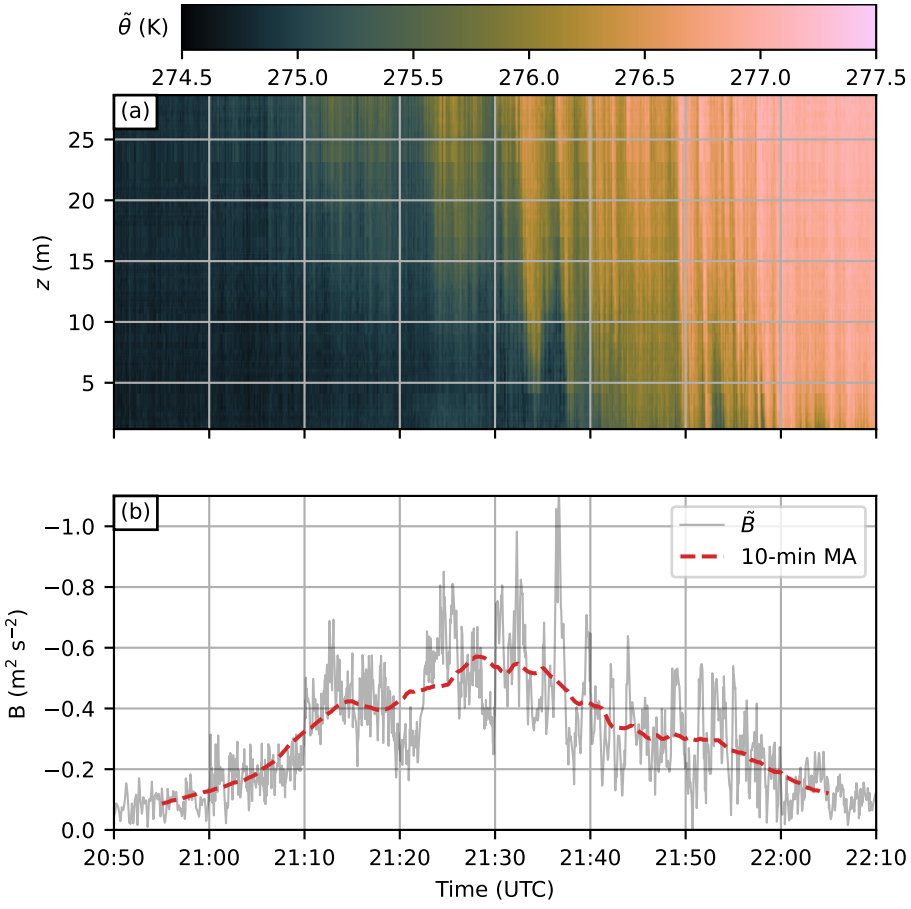

Figure 8. (a) De-noised high frequency potential temperature ($\tilde{\theta}$) time series for the event on 27 January 2020. Linear interpolation was used to interpolate the data gaps along the fibre caused by fibre attachment point interference. (b) Column-integrated buoyancy (solid grey line) over the DTS profile and the respective 10-min moving average (dashed red line).

By plotting the $\tilde{\theta}$ over the event at individual heights, it was empirically determined that a logistic function of the form

$$\tilde{\theta}(t) = \frac{\Delta\theta}{1+\exp\left(-k\left(t-t_0\right)\right)}, \tag{31}$$

where $\Delta\theta$ is the difference in θ before and after the event, k is the rate parameter and t_0 is the temporal midpoint parameter, describes the general temporal evolution of $\tilde{\theta}$ over the event reasonably well (demonstrated for two heights in Fig. 9a). Using this logistic regression to describe the $\tilde{\theta}$ evolution is particularly useful in this case, as it permits the analysis of the downward propagation of the inversion layer using t_0, and the gradient of $\tilde{\theta}$ in time using k. The rate parameter k increases as the inversion propagates downwards until $z \approx 6$ m, from where it starts to decrease towards the ground. The inversion layer can be estimated to propagate downwards at an average rate of 2.5×10^{-2} m s^{-1} when determined from the t_0 profile (Fig. 9c), i.e. on average the

https://doi.org/10.5194/amt-2021-428
Preprint. Discussion started: 14 February 2022

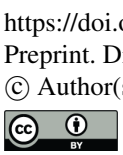

Atmospheric Measurement Techniques Discussions

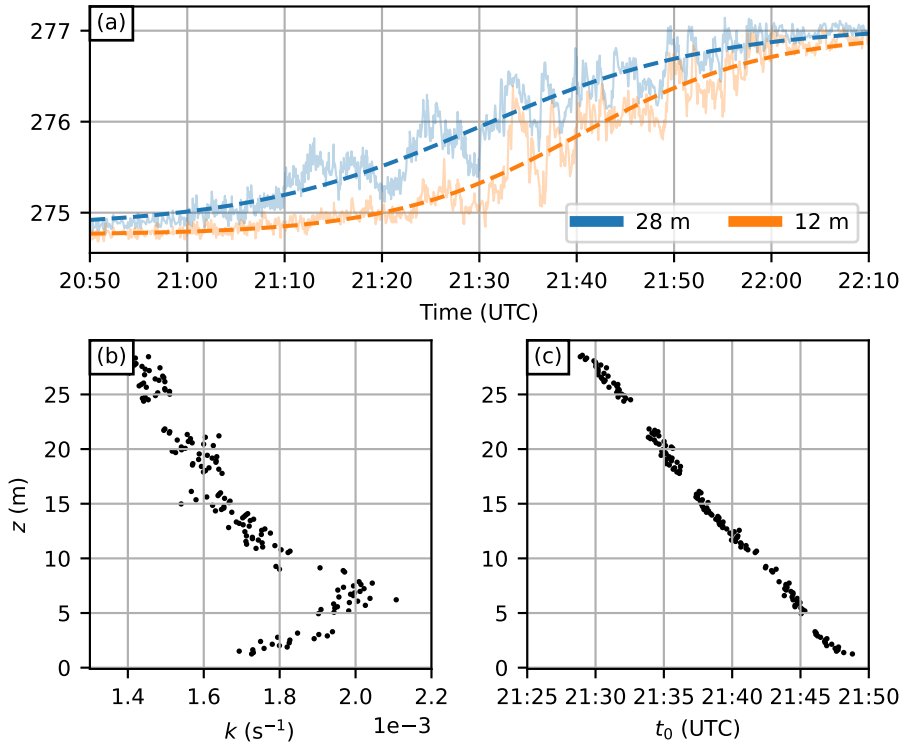

Figure 9. (a) Time series of $\tilde{\theta}$ from two heights (solid lines) and the corresponding logistic regression curve (dashed lines) for the event on 27 January 2020. (b) The rate parameter (k) of a logistic regression on $\tilde{\theta}$, as a function of height. (c) Same as b, but for the temporal midpoint parameter (t_0) of the function.

temperature curve lags 40 seconds behind the one measured from one metre above. This rate is relatively constant throughout the profile.

To study the turbulence behaviour in detail during the passage, a wavelet transform of $\tilde{\theta}$ at two heights (28 m and 12 m) was computed, with wavelet transforms of T_s measured by the sonic anemometer and the noise signal $\theta - \tilde{\theta} = \epsilon$ from respective heights for reference. The resulting wavelet-derived spectral energy density (Fig. 10a) reveals that during the event the vast majority of the DTS signal for $f > 10^{-2}$ Hz is noise. However, the spectral peaks in the EC-derived energy density supports our assertion that the scales dominant in the event lie at frequencies below $f = 10^{-2}$ Hz. The EC and DTS (28 m) spectra compare relatively well, with the major difference being a peak missing from the DTS spectrum at around $f = 8 \times 10^{-4}$ Hz (corresponds roughly to 21-min time scale). The underestimation of the variance at this scale might be caused by the fact that the de-noising algorithm was applied with a 30-min time step and hence the underestimation is not directly related to the instrument. Within the frequency band 6.2×10^{-4} Hz $< f < 1.0 \times 10^{-2}$ Hz, which contains 84% of the total temperature variance according to the EC data, the average SNR at the two heights is 3.3, a number much higher than that for the whole spectrum.

https://doi.org/10.5194/amt-2021-428
Preprint. Discussion started: 14 February 2022

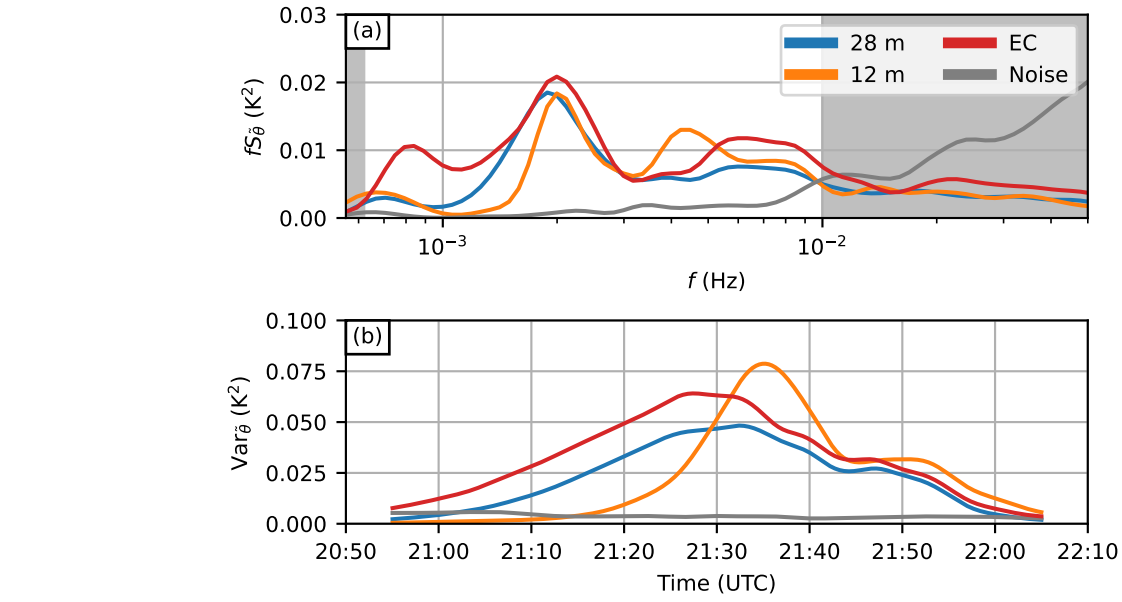

Figure 10. Wavelet analysis for the event on 27 January 2020. (a) Wavelet-derived temperature spectral energy density for DTS $\tilde{\theta}$ from two heights and for EC T_s. (b) Corresponding band-passed wavelet variance of temperature, including variance contributions only from the unshaded area of (a). 5-min running average smoothing has been applied in (b). The noise is the estimated average DTS noise at the two heights.

Reconstructing a band-passed (6.2×10^{-4} Hz $< f <$ 1.0×10^{-2} Hz) variance from the wavelet transforms (Fig. 10b) reveals a difference in the processes at 28 m and 12 m. The event is shorter-lived with higher peak thermal turbulence intensity at the lower level: the 28 m and EC variances have relatively smooth appearances between 21:05-21:45 UTC, whereas the 12 m variance increases rapidly from 21:20 UTC to a peak at 21:36 UTC and extending until 21:45, after which all three variances behave similarly. It is also worth noting that, whereas the onset of thermal turbulence at 12 m is much faster and delayed compared to 28 m, the decrease in the intensity after 21:50 UTC follows relatively similar paths at both heights.

This overall behaviour of the frontal passage can be explained with the help of these findings; during the onset phase the profile is increasingly stable, with the inversion decoupling the flow at the two heights, with no gusts able to mix the profile to neutral. However, towards the end of the event, as the warm airmass mixes downwards, some gusts are able to mix the whole profile, which increases the overall turbulent mixing across the profile. Mixing effectively leads to increasing the decay in the inversion strength, which in turn reduces the amount of negative buoyancy that a warm gust has to work against, increasing the coupling of the flow across the inversion. This can be seen as increased peak variance, shorter duration of the event (higher k and narrower variance peak), and stronger fluctuations in the observed B as the inversion progresses towards the ground. However, as no increase in the downward propagation of the inversion can be observed from the t_0 profile despite the shorter duration of the event, the depth of the inversion layer has to decrease towards the ground to compensate. This seems reasonable, as the eddy sizes associated with the mixing gusts scale with height in the surface layer, reducing the vertical length scale of the

https://doi.org/10.5194/amt-2021-428
Preprint. Discussion started: 14 February 2022


Atmospheric Measurement Techniques Discussions

eddies as the inversion layer approaches the ground. At $z < 6$ m, k decreases, possibly due to the influence of nearby vegetation or other obstacles.

3.4 Convective boundary layer development during 21-23 April 2020

Our second case study focuses on demonstrating the usability of DTS measurements in understanding convective boundary layer development on three subsequent mornings during 21-23 April 2020 (Fig. 11). All three mornings share a similar environmental setting: NNW to NNE synoptic scale flow coming over the land, clear skies and almost-equal inbound solar radiation. However, on the 22nd and 23rd, a front associated with a sea-breeze cell forming on the northern coast of the Gulf of Finland, caused by differential heating of land and sea surfaces, passes over Helsinki moving inland. During the passage of the front the low-level flow turns southerly in Helsinki and at the measurement site. Compared to the air being heated by the land, this southerly flow brings colder surface air from the sea to the coast. The passage of the sea-breeze fronts over the measurement site (the onset of the sea-breeze wind) on the 22nd and 23rd can be easily identified from the DTS $\tilde{\theta}$ time series (Fig. 12a) as a sudden halt and decline in rising values. The onset of the sea-breeze happens at approximately 07:00 UTC on the 22nd, and almost three and a half hours later at 09:20 UTC on the 23rd. The overall behaviour of the sea-breeze cell on the northern coast of the Gulf of Finland is out of scope of this article (previous studies on the matter include Savijärvi, 1985; Savijärvi et al., 2005; Gahmberg et al., 2010), but the setting causes a good opportunity to study thermal IBL caused by the discrepancy between the cold incoming marine air and solar-heated urban surface. Additionally, a day with similar setting except without the formation of a sea-breeze on the 21st provides a good baseline for comparison.

MOST-predicted B (Eqs. (18) and (20)) is generally in good agreement with the DTS-observed B during 21 April 2020 (Fig. 12b). There are two peaks not predicted by MOST, at 05:30-06:30 UTC and 08:00-09:00 UTC, but otherwise the predicted B follows surprisingly close to the observed B, given the assumptions made in MOST. However, for 22 and 23 April 2020, MOST significantly underestimates B after the onset of the sea-breeze. This indicates that the observed profile was more unstable than what was predicted with EC-estimated ζ and MOST. Such a discrepancy can be caused by a thermal IBL which has not yet grown to mast top height (Venkatram, 1986; Garratt, 1990). Figure 12c gives more indication of a developing IBL; the temperature variance at 6 m increases significantly after the onset of the sea-breeze. A similar increase is not seen at 28 m, further indicating the presence of a thermal IBL caused by the differential surface heating between urban and sea surfaces. Investigating these observed temperature profiles individually (Fig. 13) shows that the profiles for each day are very similar to each other above about 12 m. However, the negative gradient of the profiles below about 12 metres increases noticeably after the onset of the sea-breeze on the 22nd and the 23rd, indicating a possible thermal IBL corresponding to the land and urban surface.

It is also interesting to note that the two peaks in observed B mentioned earlier are common to all three days, which could be an indication of local phenomena intrinsic to the location, such as advection of air mixed from a nearby cold air pool, or more general phenomena related to the morning transition itself.

https://doi.org/10.5194/amt-2021-428
Preprint. Discussion started: 14 February 2022

Atmospheric Measurement Techniques Discussions

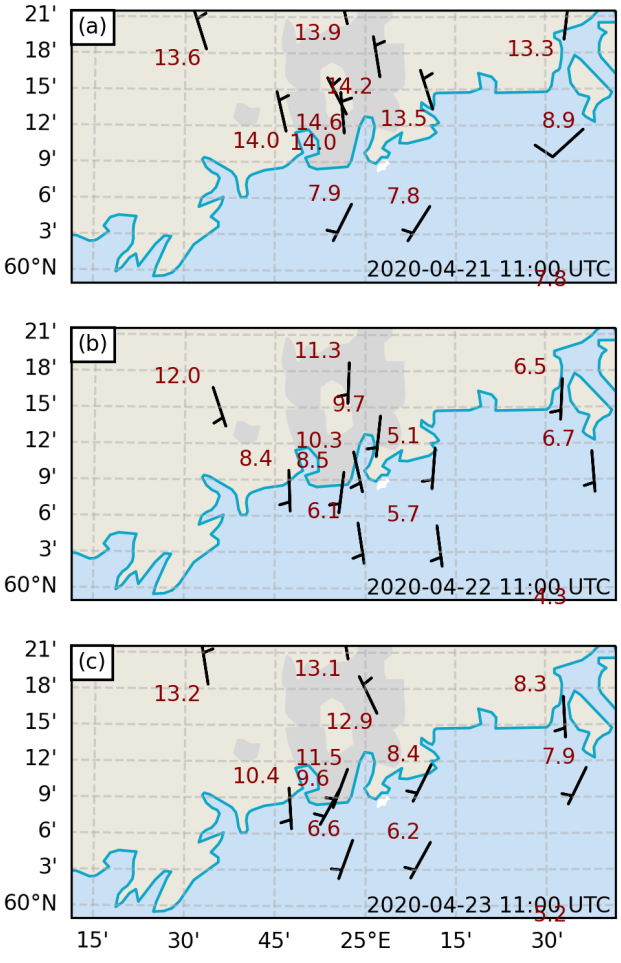

Figure 11. Surface observations of temperature and wind from official weather stations close to Helsinki at 11:00 UTC on (a) 21 Apr 2020, (b) 22 Apr 2020, and (c) 23 Apr 2020.

4 Conclusions

We have presented the results of a 14-week measurement campaign utilising high-frequency DTS temperature profile measurements at a coastal urban site, with a focus on the performance of the measurement system in varying meteorological conditions as previous studies have mainly made short-term analyses in selected meteorological conditions. Beyond performing statistical analysis over the whole measurement period, we have demonstrated the potential of the setup for studying the surface layer structure in two different meteorological scenarios.

The performance of the DTS system depends heavily on the atmospheric stability. The abundance of near-neutral conditions during the campaign severely affected the overall availability of DTS-estimated turbulence statistics. This is caused by the lack

https://doi.org/10.5194/amt-2021-428
Preprint. Discussion started: 14 February 2022

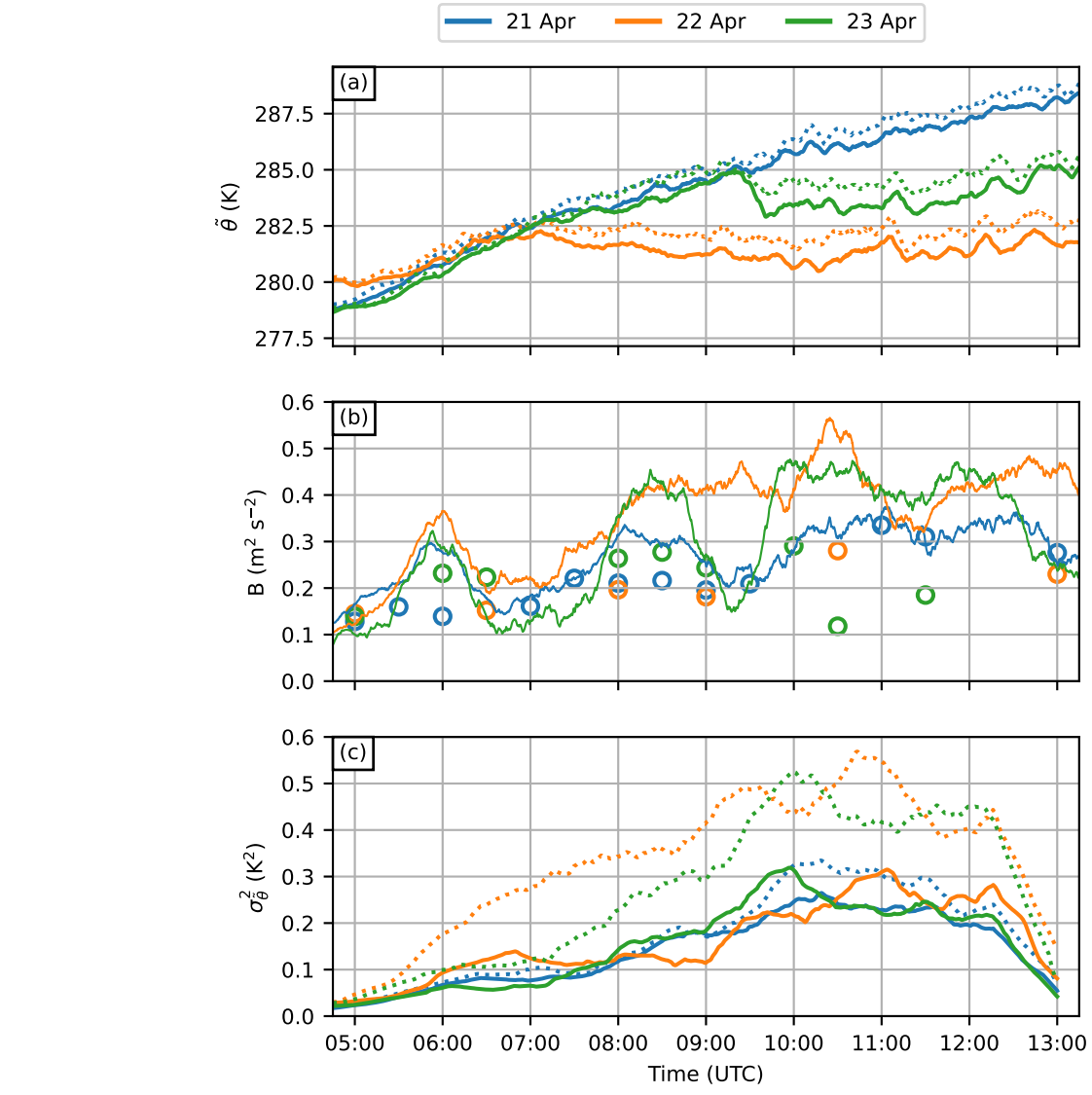

Figure 12. An overview of convective boundary layer development on 21-23 April 2020. (a) time series of $\tilde{\theta}$ estimated from the DTS system from two heights, 28 m (solid lines) and 6 m (dotted lines). (b) Column-integrated buoyancy observed using the DTS system (solid lines) and predicted using MOST (circles). Some of the predictions are missing due to flux stationarity screening performed on the EC data. (c) Wavelet-estimated localised variance estimates for 28 m (solid lines) and 6 m (dotted lines). A 10-minute moving average smoothing has been applied to the data in all panels.

of temperature fluctuations induced by buoyancy effects or mechanical forcing in near-neutral conditions, which results in the instrument SNR falling below the threshold required for the reliable estimation of second or third order statistical moments. Conditionally sampling a DTS dataset based on SNR produces a stability-wise biased dataset which will miss most near-neutral

https://doi.org/10.5194/amt-2021-428
Preprint. Discussion started: 14 February 2022

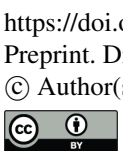

Atmospheric Measurement Techniques Discussions

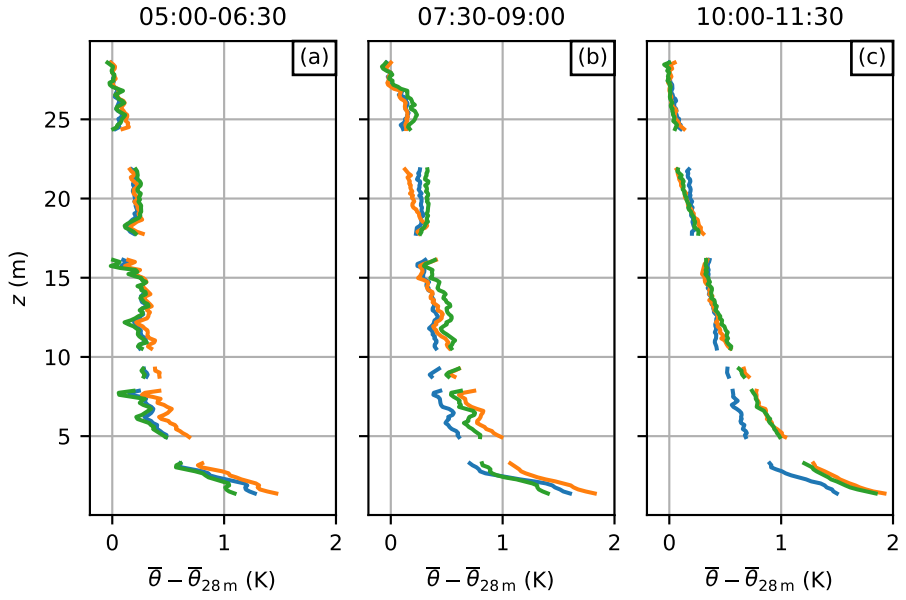

Figure 13. Observed temperature profiles for 21-23 April 2020 during three different averaging windows: (a) before the sea-breeze front has passed, (b) after the front has passed on 22 April but not on 23 April, and (c) after the front has passed the site on 22 and 23 April. The corresponding averaging intervals are given at the top of each panel.

conditions. Therefore, care must be taken when making conclusions based on such datasets. Further instrument development could mitigate this problem, as it is directly dependent on the instrument noise. Using data with high enough SNR shows that the DTS-derived temperature variance matches EC measurements well and the vertical profile follows MOST-predicted profiles surprisingly well at this complex urban measurement site. This was the first time thatthe EC measurements were shown to be measuring the constant flux layer despite the relatively short measurement mast at the site.

The first case study, focusing on a warm front mixing event, demonstrated that, through careful investigation of the scales of turbulence associated with the event, it is possible to extract useful information on turbulence and mixing processes from the DTS data even in low SNR-conditions. In this case, wavelet analysis proved useful, since it allowed the analysis of the scales relevant to the event, which were not impacted heavily by the instrument noise. Additionally, by using column-integrated buoyancy instead of individual measurements at individual heights, a more comprehensive picture of the behaviour of the temperature profile during a mixing event was possible to construct. The case highlighted the potential of the DTS system for providing new insights in the near-ground mixing of airmasses, a process not well covered by more conventional surface layer measurements.

The second case study, focusing on springtime convective boundary layer development in the presence of a sea-breeze cell, presented the possibilities for investigating the surface layer structure in the presence of an IBL with DTS. We demonstrated that DTS can capture the modification of the temperature profile due to differential surface heating between urban and sea

https://doi.org/10.5194/amt-2021-428
Preprint. Discussion started: 14 February 2022


Atmospheric Measurement Techniques Discussions

surfaces. For the non-sea-breeze case, the surface layer profile is predicted well by measurements higher in the ISL and by MOST, but is not predicted well in the presence of a sea-breeze cell. Hence, DTS measurements will help in developing better parametrisations for surface layer flows, which are required for improving the prediction of near-surface temperatures by numerical weather forecast and climate models.

Analyses of surface layer structure and turbulence often incorporate simultaneous knowledge of both the temperature and wind profiles and/or their horizontal variations. Our decision to measure only the temperature profile, supplemented by a sonic anemometer at one height, reduced the potential for further analyses of the surface layer. Hence, for further studies, we recommend supplementing the DTS profile measurements with sonic anemometers at multiple heights for evaluating other aspects of the surface layer such as turbulence production via wind shear. Furthermore, using a taller measurement mast would also aid interpretation of the surface layer structure (RSL and IBL) in varying meteorological conditions.

Code and data availability. The raw and post-processed DTS datasets are stored at https://doi.org/10.5281/zenodo.5796181 (Peltola, 2021) and the supplementary data is stored at https://doi.org/10.5281/zenodo.5793838 (Karttunen, 2021b). The Python scripts used to perform the formal analysis are stored at https://doi.org/10.5281/zenodo.5793334 (Karttunen, 2021a)

Author contributions. LJ, EO and SK conceptualised the study. LJ, OP and SK planned the DTS measurement setup. OP post-processed the raw DTS data. SK did the formal analysis and prepared the manuscript with contributions from all co-authors.

Competing interests. The authors declare that they have no conflict of interest.

Acknowledgements. This study was financially supported by the Doctoral Programme in Atmospheric Sciences (ATM-DP) at the University of Helsinki, the Academy of Finland funded CarboCity (decision 321527) and GASSTRATA (decision 315424) projects, and Atmosphere and Climate Competence Centre (ACCC, decisions: 337549 and 337552). We also thank Erkki Siivola and Pekka Rantala for helping to install the DTS system on the mast.

https://doi.org/10.5194/amt-2021-428
Preprint. Discussion started: 14 February 2022

Atmospheric Measurement Techniques Discussions

References

Andreas, E. L., Hill, R. J., Gosz, J. R., Moore, D. I., Otto, W. D., and Sarma, A. D.: Statistics of surface-layer turbulence over terrain with metre-scale heterogeneity, Boundary-Layer Meteorology, 86, 379–408, https://doi.org/10.1023/A:1000609131683, 1998.

Aubinet, M., Grelle, A., Ibrom, A., Rannik, Ü., Moncrieff, J., Foken, T., Kowalski, A. S., Martin, P. H., Berbigier, P., Bernhofer, C., Clement, R., Elbers, J., Granier, A., Grünwald, T., Morgenstern, K., Pilegaard, K., Rebmann, C., Snijders, W., Valentini, R., and Vesala, T.: Estimates of the Annual Net Carbon and Water Exchange of Forests: The EUROFLUX Methodology, Advances in Ecological Research, 30, 113–175, https://doi.org/10.1016/S0065-2504(08)60018-5, 1999.

Aubinet, M., Vesala, T., and Papale, D., eds.: Eddy Covariance, Springer, Dordrecht, 1st edn., https://doi.org/10.1007/978-94-007-2351-1, 2012.

Baars, W. J., Talluru, K. M., Hutchins, N., and Marusic, I.: Wavelet analysis of wall turbulence to study large-scale modulation of small scales, Experiments in Fluids, 56, 188, https://doi.org/10.1007/s00348-015-2058-8, 2015.

Barlow, J. F.: Progress in observing and modelling the urban boundary layer, Urban Climate, https://doi.org/10.1016/j.uclim.2014.03.011, 2014.

Bradley, S., Barlow, J., Lally, J., and Halois, C.: A sodar for profiling in a spatially inhomogeneous urban environment, Meteorologische Zeitschrift, 24, 615–624, https://doi.org/10.1127/metz/2015/0657, 2015.

Businger, J. A.: A Note on the Businger-Dyer Profiles, Topics in Micrometeorology. A Festschrift for Arch Dyer, pp. 145–151, https://doi.org/10.1007/978-94-009-2935-7_11, 1988.

Cheng, H., Hayden, P., Robins, A. G., and Castro, I. P.: Flow over cube arrays of different packing densities, Journal of Wind Engineering and Industrial Aerodynamics, 95, 715–740, https://doi.org/10.1016/J.JWEIA.2007.01.004, 2007.

City of Helsinki: 3D city model of the city of Helsinki, https://hri.fi/data/en_GB/dataset/helsingin-3d-kaupunkimalli, 2017.

de Giesen, N. V., Steele-Dunne, S. C., Jansen, J., Hoes, O., Hausner, M. B., Tyler, S., and Selker, J.: Double-Ended Calibration of Fiber-Optic Raman Spectra Distributed Temperature Sensing Data, Sensors, 12, 5471–5485, https://doi.org/10.3390/S120505471, 2012.

De Jong, S. A., Slingerland, J. D., and Van De Giesen, N. C.: Fiber optic distributed temperature sensing for the determination of air temperature, Atmospheric Measurement Techniques, 8, 335–339, https://doi.org/10.5194/amt-8-335-2015, 2015.

Emeis, S.: Surface-Based Remote Sensing of the Atmospheric Boundary Layer, Atmospheric and Oceanographic Sciences Library, Springer, Dordrecht, https://doi.org/10.1007/978-90-481-9340-0, 2011.

Epps, B. P. and Krivitzky, E. M.: Singular value decomposition of noisy data: noise filtering, Experiments in Fluids, 60, 126, https://doi.org/10.1007/s00348-019-2768-4, 2019.

Farahani, M. A. and Gogolla, T.: Spontaneous Raman scattering in optical fibers with modulated probe light for distributed temperature Raman remote sensing, Journal of Lightwave Technology, 17, 1379–1391, https://doi.org/10.1109/50.779159, 1999.

Farge, M.: Wavelet Transforms and their Applications to Turbulence, Annual Review of Fluid Mechanics, 24, 395–458, https://doi.org/10.1146/annurev.fl.24.010192.002143, 1992.

Foken, T.: Micrometeorology, Springer-Verlag, Berlin, Heidelberg, 2 edn., https://doi.org/10.1007/978-3-642-25440-6, 2017.

Fritz, A. M., Lapo, K., Freundorfer, A., Linhardt, T., and Thomas, C. K.: Revealing the Morning Transition in the Mountain Boundary Layer Using Fiber-Optic Distributed Temperature Sensing, Geophysical Research Letters, 48, e2020GL092 238, https://doi.org/10.1029/2020GL092238, 2021.

https://doi.org/10.5194/amt-2021-428
Preprint. Discussion started: 14 February 2022

Atmospheric Measurement Techniques Discussions

Gahmberg, M., Savijärvi, H., and Leskinen, M.: The influence of synoptic scale flow on sea breeze induced surface winds and calm zones, Tellus A: Dynamic Meteorology and Oceanography, 62, 209–217, https://doi.org/10.1111/J.1600-0870.2009.00423.X, 2010.

Garratt, J. R.: The internal boundary layer — A review, Boundary-Layer Meteorology 1990 50:1, 50, 171–203, https://doi.org/10.1007/BF00120524, 1990.

Hausner, M. B., Suárez, F., Glander, K. E., van de Giesen, N., Selker, J. S., and Tyler, S. W.: Calibrating Single-Ended Fiber-Optic Raman Spectra Distributed Temperature Sensing Data, Sensors 2011, Vol. 11, Pages 10859-10879, 11, 10 859–10 879, https://doi.org/10.3390/S111110859, 2011.

Higgins, C. W., Wing, M. G., Kelley, J., Sayde, C., Burnett, J., and Holmes, H. A.: A high resolution measurement of the morning ABL transition using distributed temperature sensing and an unmanned aircraft system, Environmental Fluid Mechanics, 18, 683–693, https://doi.org/10.1007/S10652-017-9569-1, 2018.

Izett, J. G., Schilperoort, B., Coenders-Gerrits, M., Baas, P., Bosveld, F. C., and van de Wiel, B. J.: Missed Fog?: On the Potential of Obtaining Observations at Increased Resolution During Shallow Fog Events, Boundary-Layer Meteorology, 173, 289–309, https://doi.org/10.1007/s10546-019-00462-3, 2019.

J. C., K. and J. J., F.: Atmospheric Boundary Layer Flows : Their Structure and Measurement., Oxford University Press, 1994.

Järvi, L., Hannuniemi, H., Hussein, T., Junninen, H., Aalto, P., Keronen, P., Kulmala, M., Keronen, P., Hillamo, R., Mäkelä, T., Siivola, E., and Vesala, T.: The urban measurement station SMEAR III: Continuous monitoring of air pollution and surface-atmosphere interactions in Helsinki, Finland, Boreal Environment Research, 14, 1797–2469, 2009.

Karttunen, S.: Python scripts for analysing distributed temperature sensing (DTS) measurements from Helsinki, Finland, https://doi.org/10.5281/zenodo.5793334, 2021a.

Karttunen, S.: Supplementary data for analysing distributed temperature sensing (DTS) measurements from Helsinki, Finland, https://doi.org/10.5281/zenodo.5793838, 2021b.

Keller, C. A., Huwald, H., Vollmer, M. K., Wenger, A., Hill, M., Parlange, M. B., and Reimann, S.: Fiber optic distributed temperature sensing for the determination of the nocturnal atmospheric boundary layer height, Atmospheric Measurement Techniques, 4, 143–149, https://doi.org/10.5194/AMT-4-143-2011, 2011.

Kotthaus, S., Haeffelin, M., Drouin, M.-A., Dupont, J.-C., Grimmond, S., Haefele, A., Hervo, M., Poltera, Y., and Wiegner, M.: Tailored Algorithms for the Detection of the Atmospheric Boundary Layer Height from Common Automatic Lidars and Ceilometers (ALC), Remote Sensing, https://doi.org/10.3390/rs12193259, 2020.

Lareau, N. P. and Horel, J. D.: Dynamically Induced Displacements of a Persistent Cold-Air Pool, Boundary-Layer Meteorology 2014 154:2, 154, 291–316, https://doi.org/10.1007/S10546-014-9968-5, 2015.

Lenschow, D. H., Wulfmeyer, V., and Senff, C.: Measuring Second- through Fourth-Order Moments in Noisy Data, Journal of Atmospheric and Oceanic Technology, 17, 1330–1347, https://doi.org/10.1175/1520-0426(2000)017<1330:MSTFOM>2.0.CO;2, 2000.

Liu, X., Tsukamoto, O., Oikawa, T., and Ohtaki, E.: A study of correlations of scalar quantities in the atmospheric surface layer, Boundary-Layer Meteorology, 87, 499–508, https://doi.org/10.1023/A:1000947709324, 1998.

Liu, Y., Liang, X. S., and Weisberg, R. H.: Rectification of the bias in the wavelet power spectrum, Journal of Atmospheric and Oceanic Technology, 24, 2093–2102, https://doi.org/10.1175/2007JTECHO511.1, 2007.

Mahrt, L., Pfister, L., and Thomas, C. K.: Small-Scale Variability in the Nocturnal Boundary Layer, Boundary-Layer Meteorology, 174, 81–98, https://doi.org/10.1007/S10546-019-00476-X, 2020.

https://doi.org/10.5194/amt-2021-428
Preprint. Discussion started: 14 February 2022

Manninen, A., Marke, T., Tuononen, M., and O'Connor, E.: Atmospheric boundary layer classification with Doppler lidar, Journal of Geophysical Research, 123, 8172–8189, https://doi.org/10.1029/2017JD028169, 2018.

Maronga, B. and Reuder, J.: On the formulation and universality of Monin-Obukhov similarity functions for mean gradients and standard deviations in the unstable surface layer: Results from surface-layer-resolving large-eddy simulations, Journal of the Atmospheric Sciences, 74, 989–1010, https://doi.org/10.1175/JAS-D-16-0186.1, 2017.

Monin, A. S. and Obukhov, A. M.: Basic laws of turbulent mixing in the surface layer of the atmosphere, Originally published in Tr. Akad. Nauk SSSR Geophiz. Inst, 24, 163–187, 1954.

Nordbo, A., Järvi, L., Haapanala, S., Moilanen, J., and Vesala, T.: Intra-City Variation in Urban Morphology and Turbulence Structure in Helsinki, Finland, Boundary-Layer Meteorology, 146, 469–496, https://doi.org/10.1007/s10546-012-9773-y, 2013.

Panofsky, H. A., Tennekes, H., Lenschow, D. H., and Wyngaard, J. C.: The characteristics of turbulent velocity components in the surface layer under convective conditions, Boundary-Layer Meteorology, 11, 355–361, https://doi.org/10.1007/BF02186086, 1977.

Päschke, E., Leinweber, R., and Lehmann, V.: An assessment of the performance of a 1.5 μm Doppler lidar for operational vertical wind profiling based on a 1-year trial, Atmospheric Measurement Techniques, 8, 2251–2266, https://doi.org/doi:10.5194/amt-8-2251-2015, 2015.

Peltola, O.: Distributed temperature sensing (DTS) measurements from Helsinki, Finland from January to May 2020, https://doi.org/10.5281/zenodo.5796181, 2021.

Peltola, O., Lapo, K., Martinkauppi, I., O'Connor, E., K. Thomas, C., and Vesala, T.: Suitability of fibre-optic distributed temperature sensing for revealing mixing processes and higher-order moments at the forest-air interface, Atmospheric Measurement Techniques, 14, 2409–2427, https://doi.org/10.5194/AMT-14-2409-2021, 2021.

Pfister, L., Sigmund, A., Olesch, J., and Thomas, C. K.: Nocturnal Near-Surface Temperature, but not Flow Dynamics, can be Predicted by Microtopography in a Mid-Range Mountain Valley, Boundary-Layer Meteorology, 165, 333–348, https://doi.org/10.1007/S10546-017-0281-Y, 2017.

Pfister, L., Lapo, K., Sayde, C., Selker, J., Mahrt, L., and Thomas, C. K.: Classifying the nocturnal atmospheric boundary layer into temperature and flow regimes, Quarterly Journal of the Royal Meteorological Society, 145, 1515–1534, https://doi.org/10.1002/QJ.3508, 2019.

Rotach, M. W.: On the influence of the urban roughness sublayer on turbulence and dispersion, Atmospheric Environment, 33, 4001–4008, https://doi.org/10.1016/S1352-2310(99)00141-7, 1999.

Savijärvi, H.: The Sea Breeze and Urban Heat Island Circulation In A Numerical Model, Geophysica, 21, 115–126, 1985.

Savijärvi, H., Niemelä, S., and Tisler, P.: Coastal winds and low-level jets: Simulations for sea gulfs, Quarterly Journal of the Royal Meteorological Society, 131, 625–637, https://doi.org/10.1256/QJ.03.177, 2005.

Sayde, C., Thomas, C. K., Wagner, J., and Selker, J.: High-resolution wind speed measurements using actively heated fiber optics, Geophysical Research Letters, 42, 10,064–10,073, https://doi.org/10.1002/2015GL066729, 2015.

Schaller, C., Göckede, M., and Foken, T.: Flux calculation of short turbulent events - Comparison of three methods, Atmospheric Measurement Techniques, 10, 869–880, https://doi.org/10.5194/amt-10-869-2017, 2017.

Schilperoort, B., Coenders-Gerrits, M., Luxemburg, W., Rodríguez, C. J., Cisneros Vaca, C., and Savenije, H.: Technical note: Using distributed temperature sensing for Bowen ratio evaporation measurements, Hydrology and Earth System Sciences, 22, 819–830, https://doi.org/10.5194/HESS-22-819-2018, 2018.

https://doi.org/10.5194/amt-2021-428
Preprint. Discussion started: 14 February 2022

Selker, J. S., Thévenaz, L., Huwald, H., Mallet, A., Luxemburg, W., Van De Giesen, N., Stejskal, M., Zeman, J., Westhoff, M., and Parlange, M. B.: Distributed fiber-optic temperature sensing for hydrologic systems, Water Resources Research, 42, https://doi.org/10.1029/2006WR005326, 2006.

Stull, R. B.: An Introduction to Boundary Layer Meteorology, vol. 13 of *Atmospheric and Oceanographic Sciences Library*, Springer Netherlands, Dordrecht, 1988.

Thomas, C. K., Kennedy, A. M., Selker, J. S., Moretti, A., Schroth, M. H., Smoot, A. R., Tufillaro, N. B., Zeeman, M. J., Thomas, C. K., Kennedy, A. M., Moretti, A., Smoot, A. R., Tufillaro, N. B., Zeeman, M. J., Selker, J. S., and Schroth, M. H.: High-Resolution Fibre-Optic Temperature Sensing: A New Tool to Study the Two-Dimensional Structure of Atmospheric Surface-Layer Flow, Boundary-Layer Meteorology 2011 142:2, 142, 177–192, https://doi.org/10.1007/S10546-011-9672-7, 2011.

Torrence, C. and Compo, G. P.: A Practical Guide to Wavelet Analysis, Bulletin of the American Meteorological Society, 79, 61–78, https://doi.org/10.1175/1520-0477(1998)079<0061:APGTWA>2.0.CO;2, 1998.

Tucker, S. C., Senff, C. J., Weickmann, A. M., Brewer, W. A., Banta, R. M., Sandberg, S. P., Law, D. C., and Hardesty, R. M.: Doppler lidar estimation of mixing height using turbulence, shear, and aerosol profiles, Journal of Atmospheric and Oceanic Technology, 26, 673–688, https://doi.org/10.1175/2008JTECHA1157.1, 2009.

Tyler, S. W., Selker, J. S., Hausner, M. B., Hatch, C. E., Torgersen, T., Thodal, C. E., and Schladow, S. G.: Environmental temperature sensing using Raman spectra DTS fiber-optic methods, Water Resources Research, 46, https://doi.org/10.1029/2008WR007052, 2009.

Venkatram, A.: An examination of methods to estimate the height of the coastal internal boundary layer, Boundary-Layer Meteorology 1986 36:1, 36, 149–156, https://doi.org/10.1007/BF00117465, 1986.

Vesala, T., Järvi, L., Launiainen, S., Sogachev, A., Rannik, Ü., Mammarella, I., Siivola, E., Keronen, P., Rinne, J., Riikonen, A., and Nikinmaa, E.: Surface-atmosphere interactions over complex urban terrain in Helsinki, Finland, Tellus B, 60, 188–199, https://doi.org/10.1111/j.1600-0889.2007.00312.x, 2008.

Ward, H. C.: Scintillometry in urban and complex environments: a review, Measurement Science and Technology, 28, 064 005, https://doi.org/10.1088/1361-6501/aa5e85, 2017.

Wilson, J. D.: Monin-Obukhov functions for standard deviations of velocity, Boundary-Layer Meteorology, 129, 353–369, https://doi.org/10.1007/s10546-008-9319-5, 2008.

Zeeman, M. J., Selker, J. S., and Thomas, C. K.: Near-Surface Motion in the Nocturnal, Stable Boundary Layer Observed with Fibre-Optic Distributed Temperature Sensing, Boundary-Layer Meteorology, 154, 189–205, https://doi.org/10.1007/S10546-014-9972-9, 2015.